

Docking of Ubiquitin to Gold Nanoparticles

Giorgia Brancolini,^{†,*} Daria B. Kokh,[‡] Luigi Calzolari,[¶] Rebecca C. Wade,[§] and Stefano Corni^{†,*}

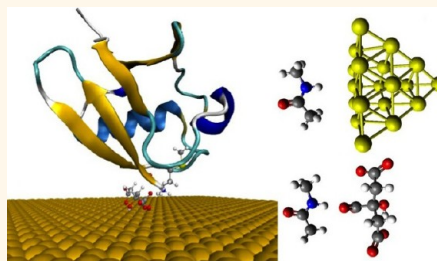
[†]Center S3, CNR Institute Nanoscience, Via Campi 213/A, 41125 Modena, Italy, [‡]Heidelberg Institute for Theoretical Studies (HITS), Schloss-Wolfsbrunnenweg 35 69118 Heidelberg, Germany, [¶]European Commission, Joint Research Centre, Institute for Health and Consumer Protection, I-21027, Ispra, Varese, Italy, and [§]Heidelberg Institute for Theoretical Studies (HITS), Schloss-Wolfsbrunnenweg 35 69118 Heidelberg, Germany and Center for Molecular Biology (ZMBH), Heidelberg University, 69120 Heidelberg, Germany

The interaction between proteins and nanoparticles (NPs) is central to many aspects of nanoscience and several nanotechnological applications. For example, the natural recognition capabilities of proteins have inspired new bottom-up approaches to the self-assembly of complex nanostructures.^{1–3} Amino acids and polypeptides have been used for the synthesis of NPs themselves,^{4–6} enabling NP shape control and yielding a biocompatible environment around the NPs. In the flourishing field of biological and biomedical applications of nanomaterials, much work is ongoing to characterize the physicochemical parameters of the interaction of NPs with proteins,^{7,8} and how they determine their biological effects,^{9–17} including potential NP toxicity.^{18–21}

Despite its relevance, a detailed structural understanding of protein–nanoparticle interactions is still elusive. Atomic-detail insights into protein–NP complexes are difficult to obtain^{7,22,23} because the high surface-to-volume ratio of nanoparticles make them physically and chemically different from the bulk, requiring nonstandard methods to probe the interface. Computer simulations at the atomistic level are a powerful tool that can effectively complement experimental studies of protein–NP and protein–surface systems.^{24–29} In particular, simulations have already proved their value for studying peptide–surface binding^{27,29–41} and amino acid driven synthesis of NPs.⁴²

In this article, we present the results of atomistic simulations on the interactions between gold NPs and the protein Ubiquitin (Ubq), obtained by using different levels of theory (*ab initio* quantum mechanical, classical Molecular Dynamics and Brownian dynamics) that cover multiple length- and time-scales. Gold NPs are an obvious choice because of their promise for a large variety

ABSTRACT Protein–nanoparticle associations have important applications in nanoscience and nanotechnology such as targeted drug delivery and therapeutics. However, the mechanisms by which proteins recognize nanoparticles and the determinants of



specificity are still poorly understood at the microscopic level. Gold is a promising material in nanoparticles for nanobiotechnology applications because of the ease of its functionalization and its tunable optical properties. Ubiquitin is a small, cysteine-free protein (ubiquitous in eukaryotes) whose binding to gold nanoparticles has been characterized recently by nuclear magnetic resonance (NMR). To reveal the molecular basis of these protein–nanoparticle interactions, we performed simulations at multiple levels (*ab initio* quantum mechanics, classical molecular dynamics and Brownian dynamics) and compared the results with experimental data (circular dichroism and NMR). The results provide a model of the ensemble of structures constituting the ubiquitin–gold surface complex, and insights into the driving forces for the binding of ubiquitin to gold nanoparticles, the role of nanoparticle surfactants (citrate) in the association process, and the origin of the perturbations in the NMR chemical shifts.

KEYWORDS: gold · nanoparticles · ubiquitin · docking · molecular dynamics · circular dichroism

of biotechnological applications⁴³ due, among other factors, to the exquisite control of shape, size, and exposed crystal faces possible with synthetic protocols.⁴⁴ Ubq has been chosen as an important and convenient model protein, being small, robust, well-characterized, cysteine-free, and biologically relevant (it is ubiquitous in eukaryotic organisms). The interaction between gold NPs and Ubq has recently been investigated experimentally by dynamic light scattering and measurements of the NMR chemical shift perturbations upon binding.⁴⁵ On the basis of the experimental data, it was concluded that Ubq forms a dense monolayer on the

* Address correspondence to giorgia.brancolini@nano.cnr.it, stefano.corni@nano.cnr.it.

Received for review July 31, 2012 and accepted October 3, 2012.

Published online October 03, 2012 10.1021/nn303444b

© 2012 American Chemical Society

TABLE 1. Resultant Encounter Complexes from Rigid-Body BD Docking of Ubq to an Au (111) Surface^a

label	RelPop % ^b	U_{repr}^c	$E_{\text{LJ}} + U_{\text{ds}}^d$	$E_{\text{LJ}} + U_{\text{ds}}^p + U_{\text{ds}}^m$	U_{EP}^f	spread ^g	contact residues ^h
A	72	-29.12	-111.58	-27.81	-1.31	1.29	GLY35, PRO37, ARG74, GLY75, GLY76
B	16	-35.74	-92.64	-37.24	1.50	0.37	PRO19, SER20, SER57, ASN60, GLN62, LYS63
C	4	-25.09	-95.44	-24.55	-0.55	0.34	GLN2, PHE4, GLY10, LYS11, THR14
D	3	-39.55	-87.24	-32.98	-6.58	0.46	LYS48, ARG54, ASP58, ASN60
E	3	-22.21	-70.14	-15.53	-6.69	0.20	SER20, THR22, GLU24, ARG54

^aA hierarchical clustering algorithm (based on a minimum distance linkage function) was applied to the diffusional encounter complexes after docking to a bare neutral gold ($\text{Au}_{\text{chg}}^{\text{net}} = 0.00 e$) surface. The reported complexes represent 98% of the encounter complexes obtained by BD simulation. ^bRelative population of this cluster. ^c U_{repr} , total interaction energy of the representative of the given cluster in kT with $T = 300 \text{ K}$. ^d E_{LJ} , Lennard-Jones energy term for the representative complex; U_{ds}^p , nonpolar (hydrophobic) desolvation energy of the representative complex, in kT . ^e U_{ds}^m , surface desolvation energy of the representative complex, in kT . ^f U_{EP} , total electrostatic energy of the representative complex, in kT . ^gRMSD of the structures within the cluster with respect to the representative complex. ^hResidues with atoms contacting gold at distances $\leq 3 \text{ \AA}$.

NPs and that Ubq interacts with gold *via* a specific protein patch.

The results of our simulations have been analyzed and compared with the published experimental data, which are here complemented by new CD and NMR measurements, thus gaining detailed insights into the Ubq–gold interactions. In particular, by using Brownian Dynamics (BD) rigid-body docking⁴⁶ and classical molecular dynamics (MD),⁴⁷ we have studied the molecular driving forces that guide the binding of Ubq to gold NPs. We have also investigated the possible role of NP surfactants (citrate in this case) in the protein–NP association process. Density functional theory (DFT) calculations have been used to investigate the physical origin of the perturbation to NMR chemical shifts upon protein binding. Besides providing valuable molecular insights, the present work also illustrates the potential for nanobioscience of multiple-level molecular calculations combined with experimental investigations.

RESULTS AND DISCUSSION

Docking of Ubq to Neutral, Bare Gold. In this section, we focus on bare NP faces, that is, we assume that the citrate surfactants⁴⁵ are removed from the NP. The role of citrate will be investigated later on in the article. We remark that naked, uncharged NP would rapidly aggregate in solution. Here we consider the binding of the Ubiquitin to a naked, uncharged surface of the nanoparticle to set a reference point for the exploration of surface charge and citrate effects later in the article. Moreover, we consider that a NP exposing an Au(111) face larger than the protein diameter (3 nm), can be approximated as a large crystalline surface. The NPs used in the NMR experiments have a mean diameter of 12 nm (for the experimental characterization of AuNP by DLS analysis, see Supporting Information); therefore the space available on the surface of a single NP is roughly 140 times that occupied by a single protein.⁴² As such, it is reasonable to assume that Ubq sees the NP locally as a flat Au surface. Among the various crystal surfaces, Au(111) is the most stable and therefore the most abundant in nanoparticles.⁴⁸

To identify possible adsorption orientations of Ubq on bare Au(111) faces (and the corresponding driving forces), we used the protein–surface docking method implemented in SDA 6.0.⁴⁹ In short, the structures of protein–surface encounter complexes were generated by running Brownian dynamics simulations during which the internal structure of the protein is kept rigid. The interaction (free) energy of the protein with the surface was obtained using the ProMetCS protein–metal continuum solvent model,⁴⁶ and adsorption free energies of Ubq on the Au(111) surface were computed for the structures resulting from the docking. The protein–surface encounter complexes obtained during a BD simulation trajectory were clustered to identify genuinely different protein orientations. For each of the most populated complexes, which were ranked by size, a representative structure was selected.

When this docking procedure was applied to the Ubq–Au(111) system with an uncharged Au surface, it yielded five different orientations accounting for more than 98% of the encounter complexes obtained, see Table 1. The representative structure of each computed complex is shown in Figure 1. The protein residues contacting the surface differ in the various complexes, and are listed in Table 1.

During docking, the interaction energy of the protein with the metal surface is described by three main terms:⁴⁶ van der Waals energy described by site–site Lennard-Jones, E_{LJ} , interactions (which also include weak chemical binding of aromatic residues, sulfur and histidine nitrogen atoms to gold), adsorbate–metal electrostatic interaction energy, U_{EP} , (dominated by the contribution from the charged side chains), and the desolvation energy of the protein, U_{ds}^p , and of the metal surface, U_{ds}^m (see Table 1). The electrostatic term arises from surface polarization and is represented by an image-charge term.⁵⁰

Binding in complexes A, B, and C is driven mostly by E_{LJ} interactions, whereas in complexes D and E electrostatic terms also contribute to binding. The difference between the binding energies in complexes A and B of $\sim 7 \text{ kT}$ comes from a more favorable surface desolvation energy for complex B. The difference between

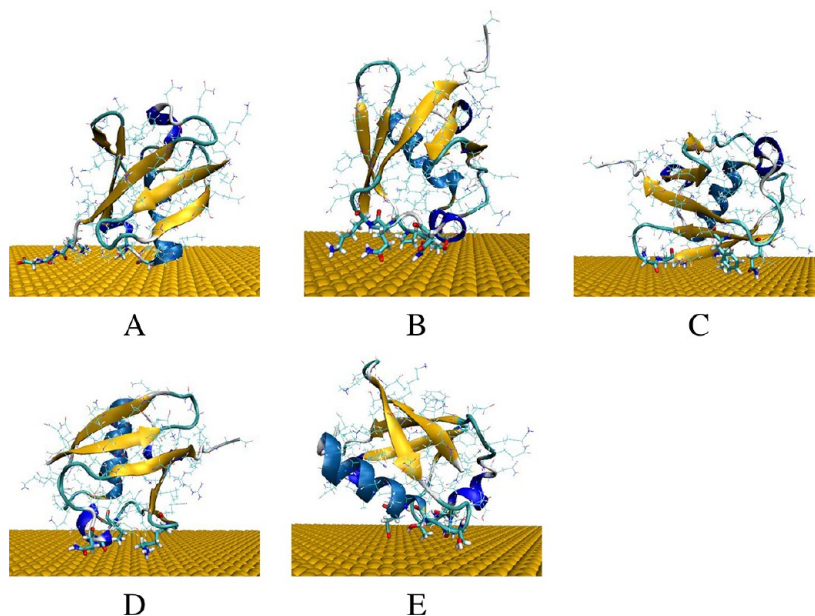


Figure 1. Most populated encounter complexes of ubiquitin on neutral gold obtained by BD simulation. The structures of representative complexes for each of the five clusters are shown, ordered by decreasing cluster size. The protein backbone is shown in cartoon representation. The residues contacting the gold surface are shown in stick representation while all other atoms are shown in line representation.

complexes B and D of ~ 4 kT mainly comes from the favorable electrostatic energy for complex D. The difference between complexes B and C of ~ 11 kT is mainly due to a more favorable surface desolvation energy for complex B. The strongest binding seems to be associated with the total amount of residues contacting the surface (see complex B in Table 1) with a small preference for LYS with respect to other aliphatic and negatively charged residues. Moreover, the contact patches do not seem to be composed predominantly of amino acids with high affinity for gold.⁴⁰ A numerical analysis of this is presented in the Supporting Information.

From the present docking results, we may conclude that Ubq on neutral gold makes two types of bound complexes: A, B, and C (the most populated) in which many contacts are used in order to optimize the binding energy, and D and E in which a small contact area is compensated by electrostatic interactions by two charged residues that simultaneously anchor the protein to the surface. Docking positions D and E appear much less than A, B, and C in the docking results, and this is because the protein is rarely able to simultaneously form two charged contacts. For D those residues are LYS48 and ARG54, as shown in Figure 2. In particular, ARG54 is able to approach the surface with the plane of its guanidinium group parallel to the Au surface and thereby to maximize its interaction with gold. This binding mode is similar to that observed for ARG residues in fibrinogen binding to a surface in MD simulations.⁴¹ The stability of such a contact, based on the fortuitously favorable orientation of the ARG side chain in the rigid protein structure, is only marginal, as we shall see in the next section.

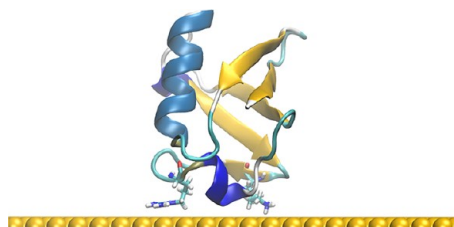


Figure 2. Structure of Ubq–Au surface complex D with ARG54 and LYS48 shown in stick representation.

Refinement of Docked Encounter Complexes by MD Simulations. To assess the stability of the docked encounter complexes and to treat protein structural relaxation, MD simulations of Ubq interacting with Au(111) in solution were performed starting with representatives of the five most populated complexes obtained from rigid-body BD docking. We first examined the stability of the docked complexes by using 20 ns of standard MD simulations at 300 K (results are reported in the Supporting Information). Because of the intrinsically limited time scale accessible to this method, it may not be able to overcome possible kinetic traps that are escapable on the experimental time scale.⁵¹ Therefore, we decided to adopt a simulation protocol that includes an initial annealing procedure, consisting of a short simulation at high temperature, to allow a more extensive search of the energy minima on the potential energy surface, PES (for details, see Methodology).⁵² The annealing protocol is not itself representative of the biological process of protein–surface binding. Simulations are based on the GoIP⁴⁷ force field with the SPC/E water model as implemented in the GROMACS

package.⁵³ This force field is compatible by construction with the ProMetCS implicit solvent model⁴⁶ used for rigid-body docking.

We first verified that the simulated annealing protocol does not affect the native structure of Ubq in solution (see Supporting Information). For each of the five most populated protein–Au(111) complexes, simulations were repeated five times using a different seed for the initial velocity distribution (d1, d2, d3, d4, d5). The results are summarized in Table 2. The potential energy components for each run were analyzed and are reported in the Supporting Information.

The MD refinement of the predicted docking complexes is discussed below, referring to Table 2.


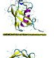


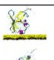

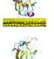

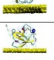









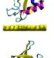


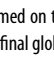

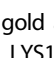
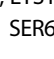
Complex A. The system remained stable in three annealing runs (d1, d2, d3, d4) and Ubq changed orientation in two (d3, d5). This result reflects the fact that the population and stability of this orientation partially rely on the initial conformation of the C-terminal tail which can be affected by conformational relaxation of the C-terminus during MD refinement. For the initial conditions, d3, the Ubq reoriented to a new orientation with the α helix nearly parallel to the surface, labeled complex G, and shown in Figure 3. The binding of Ubq to gold in this orientation is stabilized by a single contact *via* GLU24 and strengthened by THR22, ASN25, ALA28, and GLN31. The residues of the C-terminal tail, except for ARG74, are excluded from binding. Energetically, the complex is not more stable than complexes with binding mediated by the C-terminal residues (LEU71, LEU73, ARG74, GLY75) due to a less favorable E_{\perp} term for the entire complex (see Figure 2 in the Supporting Information).

For complex A-d5, strong fluctuations of the C-terminus turn the tail away from surface and allow the protein to bind through the terminal part of the α helix, that is, GLN31, ASP32, LYS33, GLU34, GLY35, and LYS11, assuming a conformation similar to complex C, labeled C', and shown in Figure 3. This minimum on the energy landscape is less energetically favorable than the others for complex A, due to the small E_{\perp} term.

Complex B. In the five independent annealings and MD runs, the system was stable with the same global orientation of Ubq with respect to the Au(111) surface. Structural relaxation of the protein affects the regions of small turns and of the 3_{10} helix which cannot be ascribed to the interaction with the surface as it is far from it. Residues MET1, GLU18, PRO19, SER20, SER57, ASP58, LYS63, GLN62, and ASN60 bind to the surface at the end of the simulations. Even when extending the length of the simulation (at $T = 300$ K) to 30 ns, the global orientation of the protein and the interacting residues were conserved.

Complex C. Sampling the conformational space around the initial complex resulted in five conformations very close in energy to each other. The global orientation of the protein with respect to the surface was maintained

TABLE 2. Orientations of Ubq on the Au (111) Surface Obtained Following the Simulated Annealing Protocol^a

Complex Num	Init. Vel.	Global orientation	
Complex A	d1	stable	
Complex A	d2	stable	
Complex A	d3	converted to G	
Complex A	d4	stable	
Complex A	d5	converted to C'	
Complex B	d1	stable	
Complex B	d2	stable	
Complex B	d3	stable	
Complex B	d4	stable	
Complex B	d5	stable	
Complex C	d1	stable	
Complex C	d2	stable	
Complex C	d3	stable	
Complex C	d4	stable	
Complex C	d5	stable	
Complex D	d1	converted to F	
Complex D	d2	converted to A	
Complex D	d3	converted to F	
Complex D	d4	converted to A	
Complex D	d5	converted to A	
Complex E	d1	top of box	
Complex E	d2	stable	
Complex E	d3	stable	
Complex E	d4	stable	
Complex E	d5	stable	

^a A series of five simulations (2 ns annealings + 10 ns MD) were performed on the representative of each complex, each with different initial velocities. The final global orientation of the systems after the simulation is reported.

in all cases. Residues at 3 Å distance from the gold at the end of the dynamics are: PHE4, THR9, GLY10, LYS10, THR12, PHE45, ALA46, GLN62, LYS63, GLU64, SER65, THR66, HIS68.

Complex D. The simulations revealed the global instability of complex D which can easily be converted into two of the other stable docking complexes, either A or a new complex, labeled complex F, and shown in Figure 3. This complex also results from rigid-body docking to the neutral gold but it is only marginally populated. The reason is that this complex has the

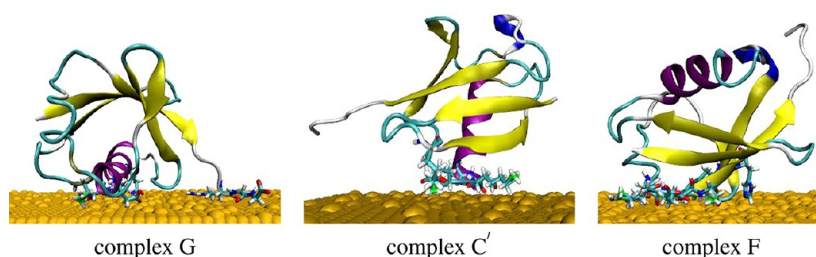


Figure 3. Complex G is a new orientation resulting from MD refinement of complex A (initial velocity d3) on a neutral gold surface. Complex C' is obtained by MD annealing of complex A (initial velocity d5) and it is also relevant for the description of Ubq binding to uncharged and positively charged gold in the presence of a negative citrate. Complex F is the orientation obtained by MD annealing of complex D (initial velocities d1,d3) on a neutral gold surface, and it is also relevant for the description of Ubq binding to a negatively charged surface.

smallest E_L term and the smallest difference between the E_L and U_{ds}^m terms. Its population becomes more significant in the presence of charged surfaces, as will be shown in the section *The Effect of Citrate on Ubq–Gold Surface Binding*. Simulations with initial velocity seeds d2, d4, and d5, showed strong fluctuations of the C-terminal tail which could anchor to the gold surface, inducing a global rotation of the protein with respect to the surface. The final complexes resulting from these simulations are very similar to complex A, binding the surface through residues of the C-terminus. For example, complex D-d2 shows a contact patch THR9, GLY35, ILE36, PRO37, ASP39, GLN40, LEU71, ARG72 in analogy with complex A. Complex D-d4 has no residues of the C-terminal tail directly contacting the gold but the α helix binds the surface, similarly to complex A-d3 but farther from the surface. Finally, complex D-d5 contacts gold with residues LEU8, THR9, GLN40, LEU71, LEU73, ARG74, GLY75, GLY76 in good agreement with complex A. On the contrary, initial velocity seeds d1 and d3 drove the protein to a global orientation characterized by a strong reorganization of its flexible turn (*i.e.*, residues ASN60, GLN62, LYS63, GLU64, SER65, THR66, HIS68, PHE45, ALA46). Complex D-d3 has contact patches involving PHE4, LYS6, PHE45, ASN60, GLN62, LYS63, GLU64, SER65, THR66, and HIS68 like the contact residues in complex F, shown in Figure 3. Complex D-d1 has contact residues: PHE45, ALA46, ASN60, GLN62, LYS63, GLU64, SER65, THR66, HIS68, in partial agreement with complex F.

Complex E. This complex is mostly stable but simulations were accompanied by a minor unfolding of the 3_{10} Helix (residues 56–59), which could be ascribed to the interaction with the surface. Some of the complexes were only marginally stable as could be seen by extending the time scale of the simulation for E-d2 when running 20 ns (instead of 10 ns) of MD, Figure 4. The contact patches of the stable complexes are very similar *e.g.* complex E-d2 SER20, THR22, GLU24, ASN25, GLY53, THR55; complex E-d4 SER20, THR22, GLY53, ARG54, THR55 and complex E-d5 SER20, THR22, GLY53, ARG54, THR55, ASP58.

Further analysis is reported in Figure 4 in which we select one refined complex for each complex and run a further 10 ns of MD. The figure reports on (a) backbone RMSD of the last 5 ns for the refined complex relative to the initial crystal structure and the comparison of (b) the initial orientation from rigid-body docking with (c) the final orientation from MD. Figure 4a shows that the divergence of each refined structure (excluding the C-terminal tail) with respect to the starting crystal structure is always between 1.5 and 2.0 Å in the last part of the 20 ns MD which points to negligible internal rearrangements. This finding is supported by experimental CD spectra measured for Ubq in solution and upon addition of gold nanoparticles, whose similarity demonstrates negligible changes in the Ubq structure Figure 5. In all reported cases, the RMSD reaches a plateau within 20 ns, meaning that after reorganization from the starting conformation, the trajectories reach an equilibrium structure, which can then be characterized by performing clustering analysis. The values of the RMSD between the representative structures of each complex are small in all selected cases, ranging from 0.62 and 0.93 Å.

To summarize, with a large number of independent MD annealing runs, we were able to discern three stable complexes (B, C, E) and one complex that was not always stable (A) out of five global orientations predicted by rigid-body BD docking.

The Effect of Citrate on Ubq–Gold Surface Binding. Citrate is one of the most common Au NP surfactants, being used during NP synthesis to prevent aggregation, and it is present on the NPs during the Ubq binding experiments.⁴⁵ Since citrate does not bind strongly to gold, it might be fully or partially replaced by the protein upon binding. In this section, we illustrate how comparative analysis of docking and experimental results can provide hints on the ability of the protein to displace (or not to displace) the citrate molecules from the NPs. To investigate the nature of the binding of Ubq to a citrate-coated gold surface,⁴⁵ as well as the effect of a negative surface potential, we introduced a small negative charge density of ($Au_{chg}^{net} = -0.01$ e) per surface atom. In this way, we implicitly included the

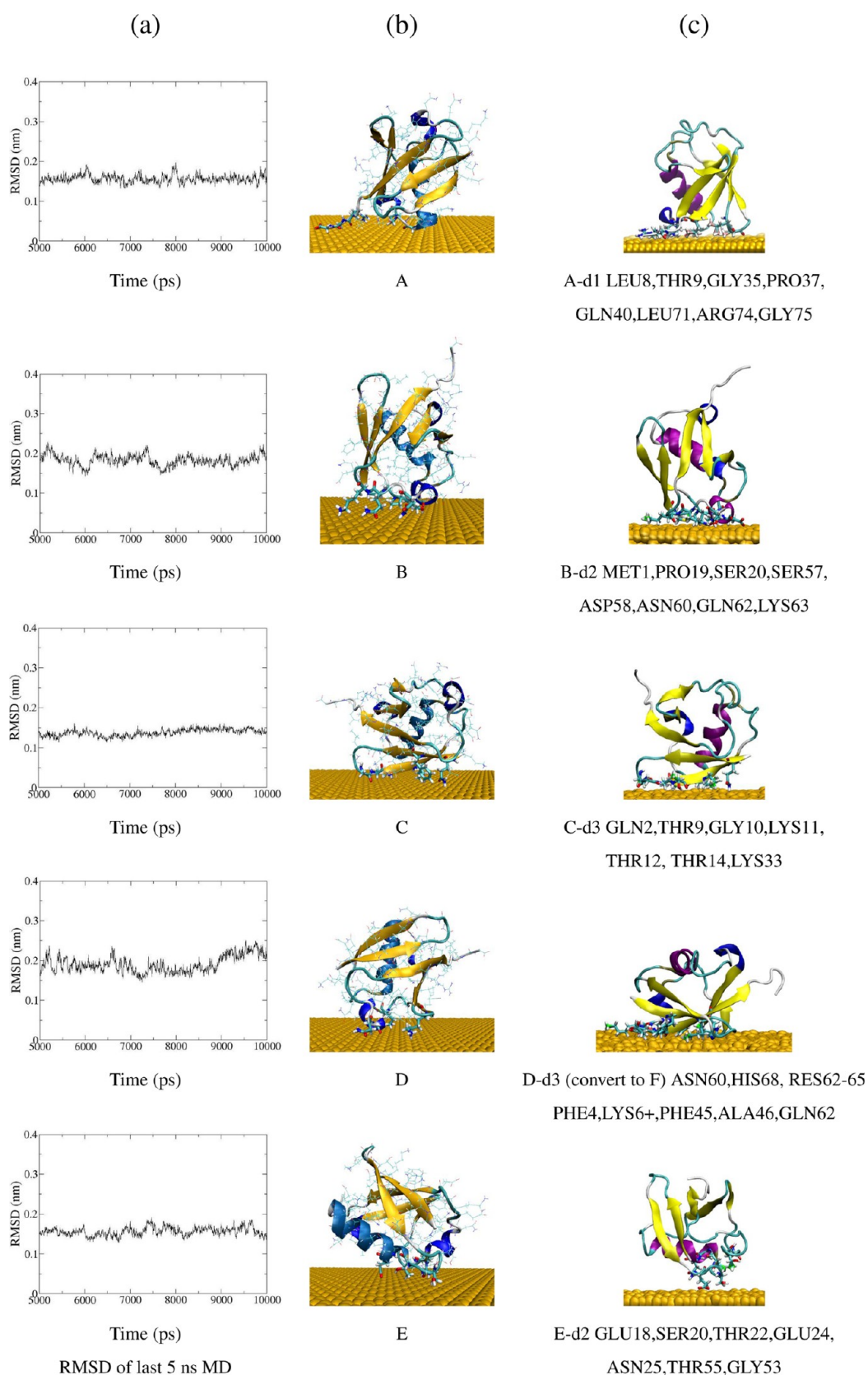


Figure 4. The most stable orientations of Ubq for each complex after 2 ns annealing and 20 ns MD at $T = 300$ K. (a) RMSD during the last 5 ns of MD using the initial structure as a reference, (b) initial orientation from docking, (c) final orientation after annealing and MD.

electrostatic effects of negatively charged citrate molecules on the surface. In what follows, an explicit citrate molecule on the Au surface will be also considered. The charge per Au atom used in the calculation was determined assuming an ordered monolayer of fully deprotonated citrate molecules.⁵⁴ The docking results in Table 3, indicate that the surface charge has a modest influence on the binding complexes already identified in Figure 1. Nevertheless, electrostatics play a role in changing the relative stability of the most populated and stable complexes. Complex B is stabilized *via* LYS63 and complex C *via* LYS11, in the presence of the negative surface. Complex F interacts *via* two lysines (LYS6 and LYS63) with an obvious electrostatic benefit which is accompanied with a significant increase of its ranking on negatively charged gold compared to the uncharged surface where it was not among the most populated complexes. Complex D interacts *via* ARG54 and LYS48 and it also benefits from electrostatic interactions with the negatively charged surface.

Thus, from Table 3, we can conclude that the Au surface charge does not affect the orientations corresponding to the local minima on the binding energy landscape (*i.e.*, most of the orientations remain the same as for the uncharged surface). However, the binding energy at the local minima can change by up to ~ 9 kT, for example, when several charged residues of the same sign contact the surface, as in complexes D and F, for positively charged residues. It also seems that the population of a complex is higher if the

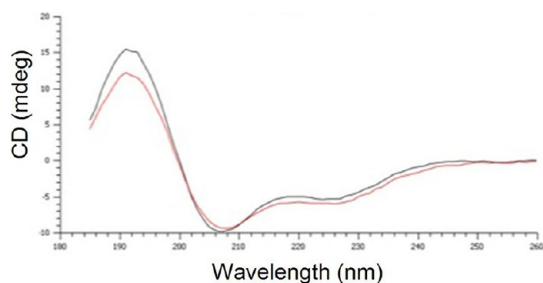


Figure 5. CD spectra for Ubq: red, free human ubiquitin; black, human Ubiquitin with AuNP.

electrostatic term is smaller (comparing complexes with similar total binding energy). This means that energy minima favored by electrostatic potential are narrower than those resulting from E_{LJ} interactions only. This observation is also supported by MD results. To model the influence of the citrate anions on binding, we also docked Ubq to a neutral gold surface in the presence of a fully deprotonated citrate anion ($C_3H_5O(COO)_3^-$). Selected encounter complexes with Ubq are shown in Figure 6.

The docking results on neutral gold with a negatively charged citrate, showed that citrate has only a modest influence on binding orientations but that it affects the binding populations. The relative populations become $A > D > F > C' > B > C$, accounting for the sampling of the encounter complexes during the BD runs. The main difference concerns complexes C and F which become very close in energy in the vicinity of a citrate anion. The reason is that complex F is favored by the interaction with the citrate *via* the E_{LJ} term which improves its ranking, whereas complex C is disfavored by electrostatic interactions with gold and its ranking is decreased. On the contrary, binding in the presence of citrate favors complex C' (see Figure 3), which becomes stable and highly populated with respect to complex C. Complex C' is very similar to complex C, in which binding of the α helix to the surface is mostly driven by electrostatic interactions. Next, we analyze how the presence of a citrate molecule in the vicinity of the protein modifies the binding energies and populations of the C' complex which is very highly populated and stable in the presence of the citrate anion. In complex C'_{close} the protein contacts the citrate at 3.5 Å and in complex C'_{far} the citrate lies at 10 Å from the protein. Complex C'_{close} binds the citrate *via* GLN2 and PHE4. The difference in the binding energies in C'_{close} and C'_{far} is 10 kT due to contributions from both the E_{LJ} (3 kT) and the electrostatic (4 kT) terms. In both cases, the protein interacts with gold through LYS11, THR14, GLU16, ASP32, and LYS33 residues. Binding in complex D is mainly driven by electrostatic interactions and its ranking and stability are improved due to interactions with citrate. In complex D_{close} the protein contacts the citrate at 4.0 Å

TABLE 3. Rigid-Body Docking Results for Ubq Binding to a Negatively Charged Au Surface^a

label	RelPop % ^b	U_{repr} ^c	$E_{LJ} + U_{ds}^p$ ^d	$E_{LJ} + U_{ds}^p + U_{ds}^m$ ^e	U_{EP} ^f	spread ^g	contact residues ^h
A	30	-26.23	-112.09	-31.86	5.63	1.50	GLY35, PRO37, ARG74, GLY75, GLY76
B	20	-35.36	-90.02	-34.55	-0.81	0.39	PRO19, SER20, SER57, ASN60, GLN62, LYS63
C	18	-27.15	-94.06	-23.18	-3.98	1.37	GLN2, PHE4, GLY10, LYS11, THR14
F	15	-28.43	-91.12	-15.55	-12.87	0.33	LYS6, ALA46, GLN62, LYS63, GLY47
D	9	-46.07	-90.29	-34.53	-11.54	0.49	LYS48, ARG54, ASP58, ASN60

^a A hierarchical clustering algorithm (based on minimum distance linkage function) was applied to the complexes after docking to a negatively charged gold ($Au_{chg}^{net} = -0.01 e$) surface. Reported complexes cover 92% of all encounter complexes obtained. ^b Relative population of this cluster. ^c U_{repr} : total interaction energy of the representative of the given cluster in kT with $T = 300$ K. ^d E_{LJ} , Lennard-Jones energy term for the representative complex; U_{ds}^p , nonpolar (hydrophobic) desolvation energy of the representative complex, in kT. ^e U_{ds}^m : surface desolvation energy of the representative complex, in kT. ^f U_{EP} , total electrostatic energy of the representative complex, in kT. ^g RMSD of the structures within the cluster with respect to the representative complex. ^h Residues with atoms contacting gold at distances ≤ 3 Å.

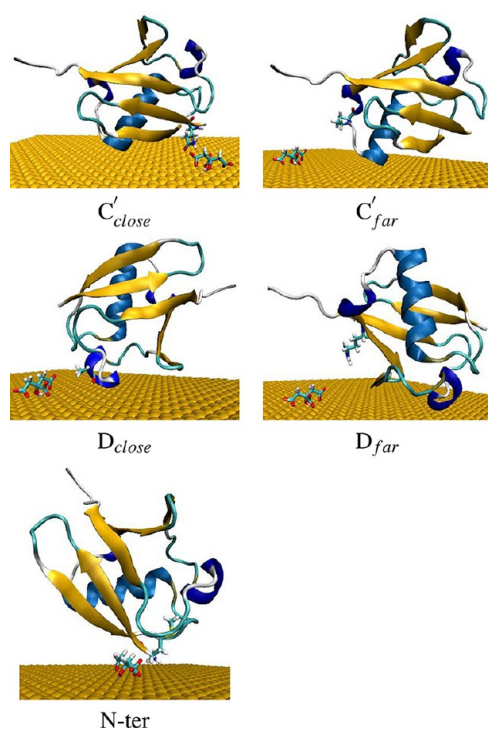


Figure 6. Rigid-body docking of Ubq to a neutral gold surface in the presence of a fully deprotonated citrate anion ($C_3H_5O(COO)_3^-$). In this case, the clustering procedure retains the relative orientation of the Ubq to the adsorbate.

and in complex D_{far} the citrate lies at 7 Å from the protein. The difference in the binding energy in complex D_{close} and complex D_{far} in Figure 6 is only ~ 3 *kT*.

The charge state of the gold surface is unclear in experiments. On one hand, citrate plus gold is certainly negative, on the other hand electrochemistry experiments indicate that citrate covered nanoparticles have positively charged gold cores.⁵⁵ Moreover, it has been already noted⁴⁵ that the experimentally identified binding patch is negatively charged, which makes the binding to a compact negative citrate layer on the gold face⁵⁶ unlikely. For completeness, we extended the docking to surfaces with opposite charges and one citrate molecule bound: negative charges on the Au surface atoms which may simulate the presence of an ad-layer of citrate, and positive charges which may account for the gold surface state upon displacement of surfactants. In the presence of negatively charged surface atoms and citrate, the ranking of the complexes became $B > A > F > C$. In the presence of positively charged surface atoms and citrate, the ranking became $A > B > C' > C > N\text{-ter}$. We remark the presence of a new complex N-ter (Figure 6), in which Ubq binds the adsorbate and the surface *via* the N-terminus. Complex N-ter also resulted from docking on a neutral surface with citrate but with a low population (data not shown). On the contrary, complex N-ter was not found for any of the bare gold surfaces without citrate.

The charge state of the gold surface does not induce new docking complexes, except for N-ter, but

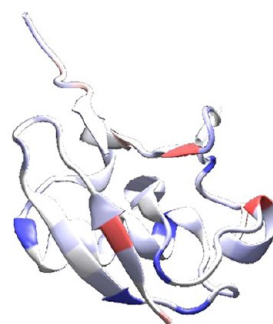


Figure 7. Cartoon representation of Ubq manually docked on an Au surface in an orientation compatible with the NMR chemical shifts.⁴⁵ The colors show the Au(111)-surface affinity of the residues (red, highest affinity; blue, lowest affinity).

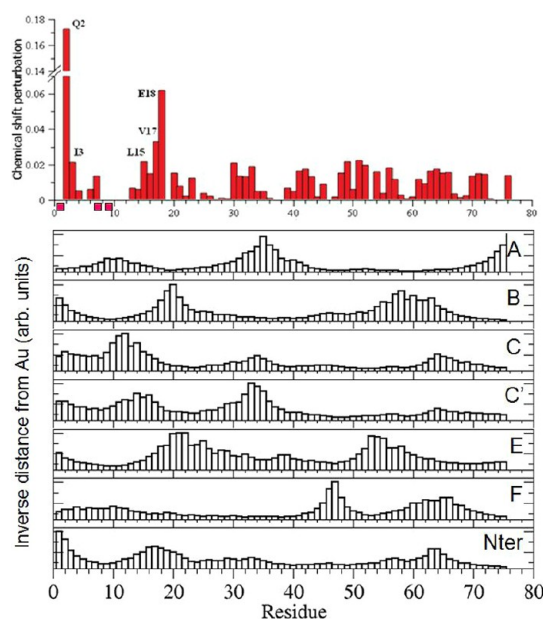


Figure 8. (Top) ^{15}N Chemical shift perturbation data for the residues of Ubq upon addition of Au NPs from ref 45. The red squares along the residue axis indicate residues for which the $^{13}C-^1H$ chemical shift perturbation is non-negligible in 2D [$^{13}C-^1H$]-HSQC experiments. (Bottom) Plots of the inverse of the distance between Ubq backbone N atoms and the gold surface for various docked complexes. Each inverse distance plot is normalized to the maximum in that plot.

is able to modify the relative populations and binding energies. As to binding strength, the neutral surface represents an intermediate case between the negative and the positive surfaces in the presence of citrate, as expected from the electrostatic contribution. Moreover, complexes B and N-ter which are compatible with experiments (in particular complex N-ter, as will be discussed in the next section), improve their ranking significantly in the presence of positively charged gold surfaces.

Comparison of Simulations with Experiments. NMR results⁴⁵ are not trivially related to single amino acid preferences for Au surface binding. This is clear from Figure 7, where an orientation specifically built to

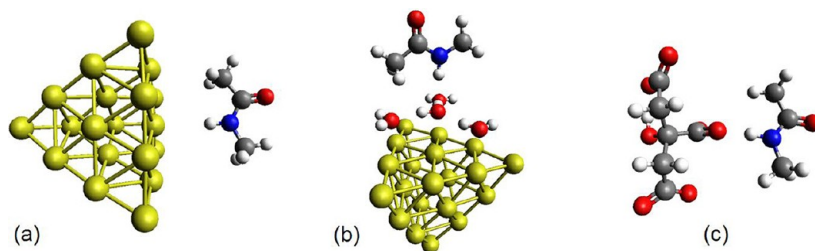


Figure 9. Model systems used to study the direct effect of Au and citrate on the ^{15}N – ^1H chemical shift of (a) NMA close to Au_{20} ; (b) same as in panel a but including four water molecules to model the structured water layer on the gold nanocrystal face; (c) NMA at equilibrium distance from citrate.

qualitatively match the NMR results is plotted with color related to the single amino acid affinity for gold (red, high affinity; blue, low affinity). From the plot, it is clear that the interacting patch is not characterized by more gold-binding residues than other parts of the protein, although we note the presence of MET1 close to the Au surface.

To qualitatively compare the complexes obtained from docking with NMR results, in Figure 8, the NMR Chemical Shift Perturbations (CSP) from ref 45 are reported along with plots of the inverse of the distances of the backbone N atoms from the gold surface for various complexes. The selected complexes refer to stable complexes with bare neutral Au after MD refinement (B, C, E, and partially A) and the most populated complexes from docking with to Au with an implicit or explicit model of citrate binding (C', F, N-ter). Regions where the CSP are high, are those most affected by the interaction with gold, and presumably, the closest to it (i.e., with the largest inverse of the distance). In Figure 8, three residues are marked by red squares indicating that they have non-negligible CSP for CH groups, as determined by 2D [^{13}C – ^1H]-HSQC experiments of the free Ubq and of Ubq after addition of gold NP. Changes in the chemical shifts for the CH moieties are few and rather small (as expected) but, after a careful analysis of the two NMR spectra, significant CSP could be identified for the following CH groups: MET1 $\text{C}\alpha\text{H}\alpha$, THR7 $\text{C}\alpha\text{H}\alpha$, THR9 $\text{C}\beta\text{H}\beta$. Our comparison will focus mostly on the patterns in residues 2–20, which contain the two high CSP regions (2–3 and 15–18), as well as the ^1H – ^{13}C perturbations.

Complexes A and F display a pattern of inverse distance peaks incompatible with experimental results. The contacts corresponding to the experimental peaks at the N-terminus and around residue 18 are absent. Moreover, for complex A, two of the three peaks of inverse distances (the second around residue 35 and the third at the C-terminus) are in regions where the NMR perturbation is low. Similarly for complex F, the peaks around residues 45 and 65 do not have experimental counterparts, whereas the experimental peaks at residues 2 and 18 have no inverse distance counterpart. The remaining complexes however show patterns compatible (although not strictly matching) with

the experimental CSP trend. Complex B has peaks at residues 1–2 and 18–19 but would also be expected to display a strong perturbation in the region around residue 60. Complex C has a large inverse distance in the residue range 1–16 with minor contributions in other regions (around residues 32 and 62). Complex C' has a qualitatively similar pattern to complex C, although the contributions further along the sequence (in particular, the peak at residues 32–34, which is also present in complex A) are higher and therefore less consistent with experimental data. Complex E is qualitatively similar to complex B but with peaks shifted to residues 19–21 and 53–55. Finally, we note the similarity between the N-ter complex pattern and the experimental data. In complex N-ter, the maxima in the inverse distances are located at residues 1 and 17, very close to the maxima in experimental CSPs (at residues 2 and 18). N-ter is the only complex where the inverse distance at residue 2 is the largest. However, as for the other complexes, complex N-ter also has a region (around residue 63) where the inverse distance is high but the experimental CSPs are small.

From this analysis, it is evident that the computational docking yielded plausible orientations among the most populated complexes. Moreover, we can infer further information on the protein binding from the analysis presented above of the effect of citrate on the docking results. We have shown that the explicit presence of a citrate anion induces the complex N-ter, which best agrees with the experimental data. In all, the results for docking on a positive gold surface with explicit citrate yield the greatest number of orientations compatible with the experimental NMR data (the relatively larger population of complex N-ter, and the high population of complexes B, C, and C'). This result suggests that at least some citrate molecules remain on the Au surface upon Ubq binding. This result would also reconcile the maintenance of the Ubq fold upon Au NP binding in the NMR experiments⁴⁵ with the known unfolding tendency of proteins on bare protein nanoparticles.⁵⁷

Origin of the NMR Chemical Shift Perturbations. One of the questions raised by the experiments⁴⁵ regards the origin of the CSPs upon binding of Ubq on gold NPs. In previous work on solid state NMR for peptides on silica, CSPs have been attributed to the vicinity to the

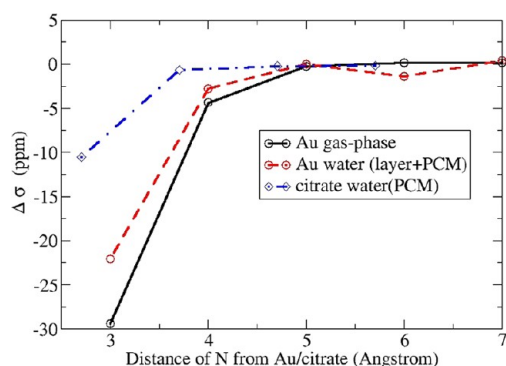


Figure 10. Change in chemical shift of ^{15}N in NMA as a function of the distance from the Au_{20} face ("Au gas-phase", "Au water (layer+PCM)") and from citrate ("citrate water (PCM)"). Gas-phase refers to results obtained by neglecting solvation effects, "water (PCM)" refers to calculations including water as a solvent with the PCM implicit solvent model and "Au water (layer+PCM)" refers to calculations including a layer of explicit water molecules and the implicit PCM water.

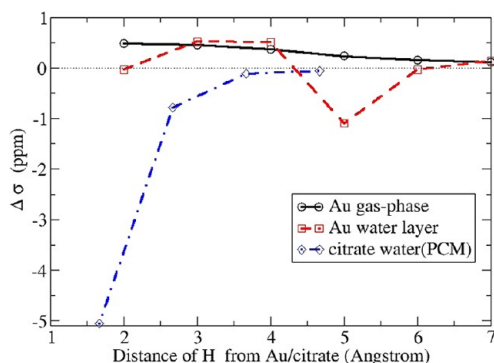


Figure 11. Change in the ^1H chemical shift of NMA as a function of distance from the Au_{20} face ("Au gas-phase" and "Au water (layer+PCM)") and from citrate ("citrate water (PCM)"). Gas-phase refers to results obtained by neglecting solvation effects, "water (PCM)" refers to calculations including water as a solvent with the PCM implicit solvent model and "Au water (layer+PCM)" refers to calculations including a layer of explicit water molecules and the implicit PCM water.

negatively charged silica surface.⁵⁸ The simulations presented in this section strengthen the assumption that Ubq CSPs arise from the proximity to the NP, that is, high CSPs indeed indicate N–H groups close to the surface. We analyzed various mechanisms by which the gold NP can induce CSPs in a nearby protein patch: (i) the gold NP locally modifies the magnetic field and thus the protein chemical shifts; (ii) the presence of highly charged molecules on the NP surface, such as citrate, modifies the local chemical environment of the contacting residues, thus affecting the chemical shifts; (iii) when the protein contacts the NP, solvent is excluded from the interface,⁴¹ which perturbs the chemical shift; (iv) the interaction with the NP affects the protein binding patch conformation which, in turn, affects the chemical shifts.

Mechanism (i). To test the effects of the presence of gold in the local environment of an N–H group, we

performed quantum mechanical calculations based on the Density Functional Theory (DFT) approach. We considered a minimal system that, without being quantitative, allows estimation of the order of magnitude of the effect: *N*-methylacetamide (NMA) close to an Au_{20} cluster (see Figure 9). NMA has been used before as a model system to study the effect of the solvent on chemical shifts.⁵⁹ Details of the calculations are in the Methods section. From the calculations, we extracted $\Delta\sigma$, the change in the chemical shift when NMA approaches gold with respect to NMA alone. The results are reported in Figure 10 for ^{15}N and in Figure 11 for ^1H . The experimentally measured CSPs were smaller than the values we get from our DFT $\Delta\sigma$. In fact, calculating CSPs from DFT results using the empirical formula⁴⁵ $\text{CSP} = [(\Delta\sigma_{\text{H}})^2 + (\Delta\sigma_{\text{N}}/5)^2]^{1/2}/2$, we obtain CSP values of the order of 1 ppm for distances around 4 Å, while the maximum experimental CSP are approximately 0.2 ppm (the second largest is approximately 0.06 ppm). This discrepancy can be understood considering that the measured NMR chemical shifts are weighted averages of bound and unbound protein.^{60,61} Under the experimental conditions used, there is an excess of unbound protein relative to bound protein in the Ubiquitin–AuNP complex, thus resulting in a scaling down of the measured chemical shift perturbation.

Finally, to verify whether the size and shape of the Au cluster can qualitatively affect these results, we performed one calculation with an Au_{48} cluster, corresponding to that used for an investigation of amino acid adsorption.⁶² The calculation was performed with N and H at a distance of 3 Å from the Au(111) surface of Au_{48} , and the calculated shifts were $\Delta\sigma_{\text{N}} = -15.1$ ppm and $\Delta\sigma_{\text{H}} = 0.87$ ppm, qualitatively similar to the Au_{20} results.

Mechanism (ii). To verify whether the interaction with citrate molecules can also affect the HN chemical shift, we calculated σ for NMA at various distances from a fully deprotonated citrate molecule. The minimum distance is that of the equilibrium structure as obtained by geometry optimization, where the NH group is hydrogen-bonded to the central carboxylate group of citrate. All these calculations include the water solvation effects *via* the polarizable continuum model (PCM).⁶³ It is clear that when the NMA–citrate H-bond is present, the chemical shifts of both N and H are affected. However, when the distance is increased by as little as 1 Å, the influence of citrate is dramatically decreased. Therefore, we do not see any sign of long-range effects related to the interaction with citrate. This is to be compared with the effect of gold, which is greater and longer range. It is to be remarked that our simple model is inadequate to represent all the peptidic NH groups in the protein, that can differ in H-bond pattern, orientation, local backbone conformation, local electrostatic potential, etc. As such, we cannot

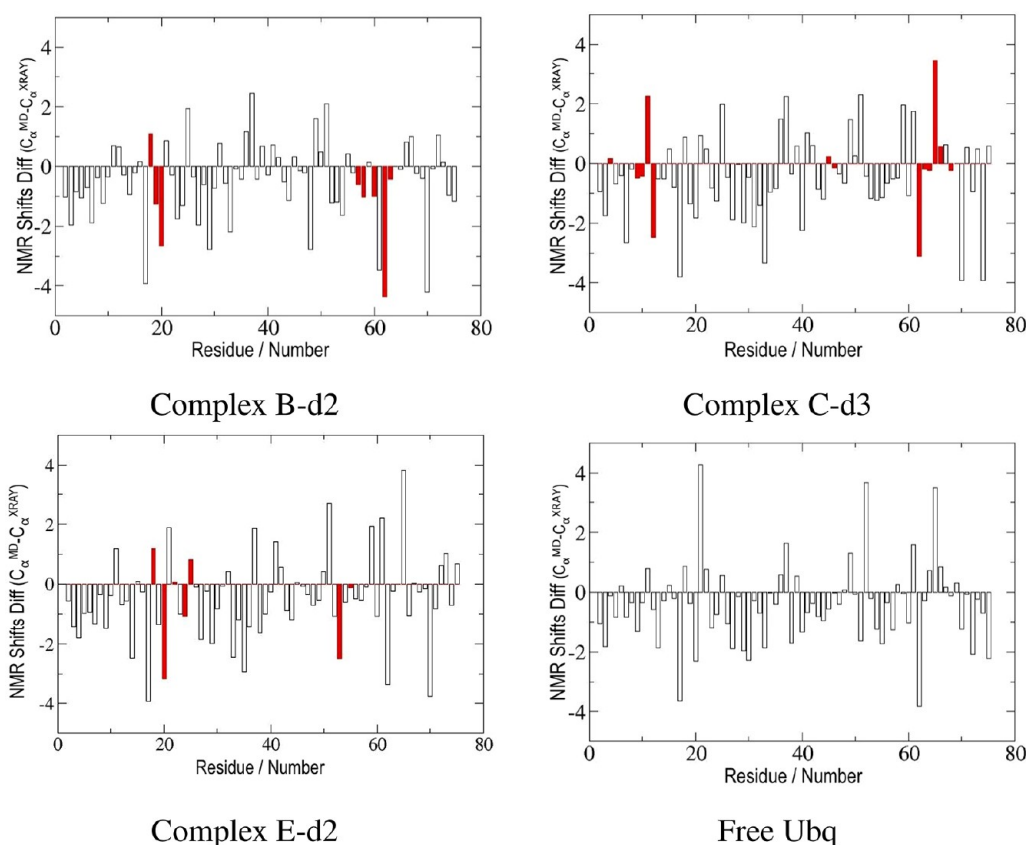


Figure 12. NMR chemical shift differences for $C\alpha$ atoms due to protein conformational changes relative to the X-ray structure of Ubq. For each complex, the difference is taken between the chemical shift computed for the structure at the end of the corresponding MD simulation and that computed for the reference X-ray structure (1UBQ.pdb). Data are reported for the three most populated complexes (A, B, and E). Red bars indicate the residues at interacting distance with the gold surface in each complex.

quantitatively predict the various $\Delta\sigma$ values obtained in experiments. Here, we simply demonstrate that the direct interaction with the gold NP and, to a lesser extent, with citrate surfactants, gives measurable perturbations of chemical shifts in the protein region contacting the NP.

Mechanism (iii). To estimate the indirect effects of gold due to the removal of water when the protein approaches gold, we have used the PCM implicit solvent model plus four explicit water molecules (Figure 9b). Such molecules model the structured nature of liquid water close to gold,⁴⁶ and their relative arrangement reproduces, for the central water molecule, the most frequent orientation and H-bond network seen in a recent *ab initio* MD simulation.⁶⁴ The removal of water is simulated by removing the explicit water molecules as soon as any of the NMA atoms would come closer to any of the water atoms than their van der Waals distance. This happens for a gold– N_{NMA} distance of approximately 4.8 Å, therefore in Figure 10 and Figure 11, all the in-water results for distances equal to or greater than 4.8 Å include explicit water molecules, all the others do not include them. In contrast to the *in vacuo* results, the $\Delta\sigma$ trends are not monotonic with the distance to gold: moving from

large to small distances to gold, NMA feels the specific interaction with the water molecules^{59,65} that is responsible for the dip at 6 Å (5 Å) for the N (H) $\Delta\sigma$. For smaller distances, the water molecules are removed and $\Delta\sigma$ becomes comparable to gas-phase values again. We can thus conclude that water removal also has an effect on σ , at least when the backbone NH is solvent accessible.

Mechanism (iv). To investigate to which extent the CSPs are due to gold-induced protein conformational rearrangements, we performed an empirical evaluation of NMR shifts for the most stable complexes after MD refinement and we compared them to values derived with the same empirical method for the crystal structure. The values were obtained with the program SHIFTS 4.1.⁶⁶ The empirical database⁶⁷ on which the program relies, was found to be highly reliable only for $C\alpha, \beta$ but not for estimating N and H chemical shifts. For this reason, here we focus only on $C\alpha$ atoms. We report in Figure 12 $C\alpha$ NMR chemical shift differences evaluated as the differences between the values computed for the MD representative structures and that for the reference X-ray structure (1UBQ.pdb), for the complexes A, B, and E. Red bars indicate the residues at interacting distance with the gold surface in each case.

The empirical shift differences are quite small in all cases and their magnitude (max. ± 4 ppm) is comparable to those obtained for the simulated free protein in solution with respect to the X-ray structure. Such free *versus* X-ray structure differences set the error bars of this MD+SHIFTS analysis (incidentally, the backbone RMSD free with respect to the X-ray structure is a reasonably small value, 1.06 Å). As such, we can conclude that the effects on chemical shifts due to the gold-induced conformational rearrangements accessible in MD are within the error bars of our approach. It is however interesting to note that the chemical shift differences for residues 11 and 12, similar for complexes B and E and the free Ubq, are instead larger for complex C, where these residues contact the surface (measurable ^{13}C CSP in the experiment are for $\alpha\text{-C1}$, $\alpha\text{-C7}$, $\beta\text{-C9}$).

In conclusion, let us recapitulate the findings of this section. Among the various plausible mechanisms that we have analyzed to explain the origin of CSPs, we found that both the direct interactions with the AuNP and with a citrate ion are able to induce large changes in chemical shifts, compatible with experimental findings. Water exclusion upon binding has a smaller effect and would be relevant only for solvent exposed NH groups. Finally, CSPs induced by conformational changes in the binding patch appear to be minor, although the level of accuracy of our analysis does not allow a definitive conclusion regarding their role.

CONCLUSIONS

We have presented a comprehensive computational study of the interaction between Ubq and a gold NP.

METHODOLOGY

Ubiquitin–AuNP Interaction Characterization. Gold nanoparticles (AuNP) were produced by NaBH_4 reduction of a starting solution of sodium citrate and HAuCl_4 in water following a standard protocol with minor modifications (see Supporting Information) to provide AuNP in the 10–30 nm size range. The particle size distribution (PSD) of the resulting nanoparticles was measured by dynamic light scattering (DLS). DLS measurements of free, freshly synthesized nanoparticles, show that AuNP have near-monodispersed PSD with a mean hydrodynamic diameter of 12.0 nm and polydispersity index of 0.1 (Figure 1). Upon the addition of human ubiquitin the PSD of the AuNP–hUbq complex continues to show the presence of a near-monodispersed sample but now with a mean hydrodynamic diameter of 17.1 nm and polydispersity index of 0.21 (Figure 1). This indicates that AuNP are stable in the presence of ubiquitin at pH 7.7 and the addition of protein does not cause the formation of nanoparticle aggregates. The increase in hydrodynamic diameter upon hUbq addition indicates that hUbq molecules interact with the gold nanoparticles in solution. The direct interaction of hUbq with AuNP is confirmed by the shift in the plasmon resonance band of AuNP upon addition of hUbq. The UV–vis spectrum of free AuNP shows a typical intense plasmon resonance band centered at 520 nm. After the addition of human ubiquitin this band shifts to 525 nm (see Supporting Information, Figure S2). This red shift of 5 nm in the surface plasmon resonance band is in agreement with results obtained

We have used atomic detail simulations at multiple levels of theory, including docking by Brownian dynamics, classical atomistic MD and quantum mechanical DFT calculations. From these simulations, we could provide molecular insights into the Ubq–gold NP interactions that are not accessible from experiments alone. In particular, on the basis of our results on protein–surface docking, we discussed the nature of the interactions that guide the binding of Ubq to the gold nanoparticle, finding that short-range, non-electrostatic interactions and binding to citrate are the leading terms for the encounter complexes most compatible with experimental results. Moreover, the comparison between docking results obtained in various conditions (bare surface, citrate-covered surface) suggests that some citrate molecules do remain on the surface of the NP, coexisting with the adsorbed protein while others are displaced. Finally, DFT calculations indicate that the measured perturbations of the NMR chemical shifts of H and N backbone atoms stem from the direct interaction of such atoms with the gold NP and with citrate. This finding corroborates the use of NMR chemical shift perturbation measurements as a tool to identify protein binding patches to gold NPs.⁴⁵ Several other interesting issues have still to be addressed, experimentally and computationally, for systems like the one studied here, such as the role of salt concentration, pH, and protein/NP ratio in determining the resulting encounter complexes. Our work demonstrates how experimental and computational approaches can be used together to reveal basic features of the protein–nanoparticle systems that cannot be inferred from either of them alone.

on a similar system where azurin (a protein with size similar to ubiquitin) interacts with gold nanoparticles of 20 nm.

Dynamic Light Scattering (DLS). Particle size distribution (PSD) was determined by dynamic light scattering (DLS). Measurements were obtained with a Malvern Zetasizer Nano-ZS instrument with temperature control. Each sample was recorded at $25\text{ }^\circ\text{C} \pm 1\text{ }^\circ\text{C}$, in triplicate; each measurement was the average of 20 data sets acquired for 10 s each. Hydrodynamic diameters have been calculated using the internal software analysis from the DLS intensity-weighted particle size distribution.

NMR Spectroscopy. (^{13}C , ^{15}N)-labeled recombinant human ubiquitin was purchased from ProtEra s.r.l (Florence, Italy). Samples for NMR experiments were prepared by dissolving (^{13}C , ^{15}N)-labeled ubiquitin in a 15 mM phosphate buffer, at pH 7.7 with 10% D_2O to a final concentration of 50 μM . NMR experiments were performed with a 700 MHz Bruker NMR instrument equipped with a cryoprobe. 2D [^{13}C – ^1H]-HSQC experiments were performed with 2048 complex points in acquisition and 300 points in the indirect dimension. Data were processed with the same processing parameters for all samples using the TopSpin NMR software. Data analysis and peak assignment were performed with the program Cara.⁶⁸ The CH peaks of ubiquitin in the 2D [^{13}C – ^1H]-HSQC experiment have been previously assigned.⁶⁹

CD Spectroscopy. Recombinant human ubiquitin was purchased from ProtEra s.r.l (Florence, Italy). Protein samples were

prepared by dissolving them in 1 mM phosphate buffer at pH 7.0. CD spectra were collected at the beamline B23 module end-station B of the Diamond Light Source (UK). CD spectra were collected with Suprasil cells of 0.2 cm path length (Starna), with bandwidth of 1.2 nm, integration time of 1 s, 1 nm digital resolution, 39 nm/min scan speed, and 4 repeated scans per spectrum. The reported spectra were averaged, corrected by subtraction of CD spectrum of the buffer alone and smoothed by applying a seven-points Savitzky–Golay smoothing function.

Synthesis of Gold Nanoparticles. The gold nanoparticles were made by first heating 100 mL of a 2.5 mM sodium citrate solution to 96 °C in a microwave reactor (Discover S by CEM). After 5 min for temperature stabilization, 5 mL of a 10 mM solution of HAuCl₄ was injected with vigorous stirring into the sodium citrate solution and the reaction was allowed to go to completion by continued heating at 96 °C for 20 min.

Brownian Dynamics Simulations. Rigid-body docking simulations were carried out using Brownian dynamics (BD) techniques with the ProMetCS continuum solvent model for protein–gold surface interactions.⁴⁶ The calculations were performed using the SDA version 6 software.^{70,71} The Au(111) surface was constructed with a surface area of 100 Å × 100 Å and three atomic layers.⁴⁷ The Ubq structure was taken from the crystal structure solved at 1.8 Å resolution (PDB id: 1UBQ). The crystallographic *R*-factor for the final model is 0.176. Bond lengths and bond angles in the molecule have root-mean-square deviations from ideal values of 0.016 Å and 1.5 degrees, respectively. The overall structure of ubiquitin is extremely compact and tightly hydrogen-bonded. Prominent secondary structure features include three and a half turns of α helix, a short piece of 3_{10} helix, a mixed beta-sheet that contains five strands, and seven reverse turns. An experimental salt concentration of 15 mM was included as a nonspecific screening effect on the electrostatic potential of the protein which was calculated using the APBS program.⁷² All titratable protein side chains, were assigned their standard protonation state at pH 7.7 with H⁺,⁷³ corresponding to the experimental pH.⁴⁵ Next, 5000 BD trajectories were computed starting with the protein positioned randomly with its center at a distance of 70 Å from the surface where the protein–surface interaction energy is negligible. The specified number of docked complexes was extracted directly from the runs and clustered with a clustering algorithm. The relative translational diffusion coefficient was 0.0123 Å²/ps, and the rotational diffusion coefficient for the protein was 1.36×10^{-4} in radian²/ps. The simulation time step was set to 0.50 ps. Parameters for the calculation of hydrophobic desolvation energy/forces was set to -0.019 kcal/(mol/Å²) and for the electrostatic desolvation energy/forces to 1.67 according to ref 74. BD trajectories were generated in a rectangular box (ibox=1); the dimensions of the (*x*, *y*) plane, describing the symmetry of the simulation volume as well as the surface size, were given as input parameters. At each BD step, the protein–surface interaction energy and forces acting on the protein were computed using the implicit-solvent ProMetCS force field,⁴⁶ developed and parameterized for protein–gold surface interactions. The energy terms included in ProMetCS have been described in the main text.

Two clustering algorithms were tested and evaluated for this system. These were top-down splitting (hierarchical based on a reference structure) and bottom-up aggregating (single-linkage based on RMSD). When an explicit citrate molecule was not present, the results of docking were preprocessed by translating the protein coordinates parallel to the surface in order to superimpose the protein structures before applying the clustering algorithm. We selected the algorithm and parameters providing the smallest number of physically distinct orientations of Ubiquitin on Au. Thus, we applied a single-linkage clustering method (based on CA atoms, with RMSD = 3.0 Å) for all the results given in the manuscript.

Molecular Dynamics Simulations. The same protein and gold structures as for the BD simulations were used for the initial coordinates for the MD simulations. A cubic simulation box of dimension (55 Å × 55 Å × 55 Å) including SPC/E water molecules, the protein, and the gold surface was built. The protein was placed at the positions of the representatives of the docked clusters obtained from the BD docking simulations.

Before the addition of the water molecules, the center of mass of the protein was placed at 26 Å from the surface, retaining the original docked orientation with respect to the surface. The choice of this distance was motivated by various tests that we performed showing that if the simulations were started with the protein in direct contact to the surface (or at smaller distances), it was in a kinetically trapped state where only minor relaxation could take place on the time-scale of tens of nanoseconds. During equilibration dynamics, all systems contacted the surface within the first 1 ns of MD without reorienting respect to the surface.

All simulations were performed with the Gromacs 4.5.4 package.⁵³ GOLF⁴⁷ and OPLS/AA parameters⁷⁵ were used for the surface and the protein, and the SPC/E water model⁷⁶ was applied. The lengths of bonds were constrained with the LINCS algorithm. Surface gold atoms and bulk gold atoms were frozen during all simulations but gold dipole charges were left free. Classical MD simulations were performed at constant volume and temperature (*T* = 300 K). Periodic boundary conditions and the Particle-Mesh-Ewald algorithm were used. A 2 fs integration time step was used.

Five independent runs for each of the protein–Au(111) docking conformations were performed, each starting with different initial velocities (d1, d2, d3, d4, d5). The annealing simulation protocol was as follows: (i) protein and solvent were first coupled to 0 K at 0 ps, the reference temperature was then increased linearly to reach (ii) 360 K after 180 ps and (iii) the maximum temperature of 440 K at 260 ps. The temperature (iv) was kept fixed at 440 K until 360 ps and then (v) decreased to 300 K at 500 ps. After this, the temperature (vi) was kept constant at 300 K until the end of the 2 ns simulation. The Au(111) was coupled to 300 K with a Nosé–Hoover thermostat. The 2 ns annealing simulations were followed by 10 ns of standard MD simulation at a constant temperature of 300 K in the NVT ensemble. Trajectories were analyzed in terms of density, temperature, potential energy, and other macroscopic properties with the Gromacs tools (e.g., *g_traj*, *g_rms*, *g_clusters* etc.).

DFT Calculation of Chemical Shifts. The calculation of the perturbation of ¹⁵N and ¹H chemical shifts due to gold, citrate, and H-bonding to a water molecule were performed with the B3LYP hybrid functional and the LANL2DZ effective core potential and basis set using the Gaussian 09 suite of programs.⁷⁷ The structures of Au₂₀ and *N*-methylacetamide (NMA) were optimized in gas-phase at the same level of theory. NMA was then placed close to the Au₂₀ face, with the NH bond perpendicular to the surface. No geometry relaxation was attempted. Geometries with various N–Au and H–Au distances were produced by translating NMA perpendicular to the gold cluster face. The basis set superposition error (BSSE) on chemical shifts was estimated by calculating the chemical shift with ghost Au₂₀ atoms that conserve only the basis set but not the core potential of Au atoms. A test was also performed with a Au₄₈ cluster, obtained by building an Au(111) slab three layers thick and cutting it along the [110] and [101] direction, $3\sqrt{2}$ atoms wide in each direction. In the calculations involving explicit water molecules added to the NMA–Au₂₀ system (Figure 9b), four water molecules were each placed on top of a gold atom on the face of the Au₂₀, with the water molecule plane parallel to the gold face and the oxygen at a distance of 2.8 Å from the underlying Au atom. Water molecules were oriented so that the central water molecule donates two H-bonds and accepts one from the other three.

The geometry of the citrate–NMA adduct was initially created by considering the same citrate geometry and citrate orientation with respect to the surface used in the docking. This choice leaves two available H-bond acceptor sites, as the third carboxylate group is engaged with the Au surface. We choose to place NMA close to the central carboxylate moiety as in this position it can experience stronger Coulombic interactions with the other carboxylate. The geometry was optimized in an implicit (PCM) water environment with default Gaussian thresholds for determining convergence of the optimization procedures. Adducts with larger citrate and NMA distances were created by translating NMA along the citrate O–NMA H–NMA N direction with steps of 1 Å. For calculations in water, we used the IEF version of PCM^{78–80} as implemented in Gaussian 09. Default cavity parameters were employed.

Empirical evaluation of NMR shifts for the most representative structures sorted for each cluster, (using as a reference the NMR shifts of the experimental crystal structure), was performed with the SHIFT4.1 program from the Amber10 suite.

Conflict of Interest: The authors declare no competing financial interest.

Acknowledgment. The authors thank Stefan Richter (HITS) for assistance with software and Musa Ozboyaci (HITS) for helpful discussions. The authors acknowledge CINECA for an award under the IS CRA initiative for high performance computing resources and support. Funding was provided by the IIT-Platform Computational (Seed Project MOPROSURF), by MIUR (FIRB Project Italanonnet), by the EU (FP6 NEST STREP Project Prosurf, No. 028331), and by the Klaus Tschira Foundation. Computational time and facilities at CNMS (Oak Ridge National Laboratory, USA) were granted by CNMS (Project CNMS2010-034) and at CINECA (Bologna, Italy) were granted by NANOPRO.

Supporting Information Available: Additional calculations and figures as described in the text. This material is available free of charge via the Internet at <http://pubs.acs.org>.

REFERENCES AND NOTES

- Sarikaya, M.; Tamerler, C.; Jen, A. K.; Schulten, K.; Baneyx, F. Molecular Biomimetics: Nanotechnology through Biology. *Nat. Mater.* **2003**, *2*, 577–585.
- Keren, K.; Berman, R. S.; Buchstab, E.; Sivan, U.; Braun, E. DNA-Templated Carbon Nanotube Field-Effect Transistor. *Science* **2003**, *302*, 1380–1382.
- Nam, K. T.; Kim, D.-W.; Yoo, P. J.; Chiang, C.-Y.; Meethong, N.; Hammond, P. T.; Chiang, Y.-M.; Belcher, A. M. Virus-Enabled Synthesis and Assembly of Nanowires for Lithium Ion Battery Electrodes. *Science* **2006**, *312*, 885–888.
- Naik, R. R.; Stringer, J. S.; Agarwal, G.; Jones, S. E.; Stone, M. O. Biomimetic Synthesis and Patterning of Silver Nanoparticles. *Nat. Mater.* **2002**, *1*, 169–172.
- Crookes-Goodson, W. J.; Slocik, J. M.; Naik, R. R. Bio-directed Synthesis and Assembly of Nanomaterials. *Chem. Soc. Rev.* **2008**, *37*, 2403–2412.
- Dickerson, M. B.; Sandhage, K. H.; Naik, R. R. Protein- and Peptide-Directed Syntheses of Inorganic Materials. *Chem. Rev.* **2008**, *108*, 4935–4978.
- Mahmoudi, M.; Lynch, I.; Ejtehadi, M. R.; Monopoli, M. P.; Bombelli, F. B.; Laurent, S. Protein–Nanoparticle Interactions: Opportunities and Challenges. *Chem. Rev.* **2011**, *111*, 5610–5637.
- Lacerda, S. H. D. P.; Park, J. J.; Meuse, C.; Pristiniski, D.; Becker, M. L.; Karim, A.; Douglas, J. F. Interaction of Gold Nanoparticles with Common Human Blood Proteins. *ACS Nano* **2010**, *4*, 365–379.
- Maiorano, G.; Sabella, S.; Sorce, B.; Brunetti, V.; Malvindi, M. A.; Cingolani, R.; Pompa, P. P. Effects of Cell Culture Media on the Dynamic Formation of Protein–Nanoparticle Complexes and Influence on the Cellular Response. *ACS Nano* **2010**, *4*, 7481–7491.
- Cedervall, T.; Lynch, I.; Lindman, S.; Berggård, T.; Thulin, E.; Nilsson, H.; Dawson, K. A.; Linse, S. Understanding the Nanoparticle–Protein Corona Using Methods to Quantify Exchange Rates and Affinities of Proteins for Nanoparticles. *Proc. Natl. Acad. Sci. U.S.A.* **2007**, *104*, 2050–2055.
- Lundqvist, M.; Stigler, J.; Elia, G.; Lynch, I.; Cedervall, T.; Dawson, K. A. Nanoparticle Size and Surface Properties Determine the Protein Corona with Possible Implications for Biological Impacts. *Proc. Natl. Acad. Sci. U.S.A.* **2008**, *105*, 14265–14270.
- Dutta, D.; Sundaram, S. K.; Teegarden, J. G.; Riley, B. J.; Fifield, L. S.; Jacobs, J. M.; Addleman, S. R.; Kaysen, G. A.; Moudgil, B. M.; Weber, T. J. Adsorbed Proteins Influence the Biological Activity and Molecular Targeting of Nanomaterials. *Toxicol. Sci.* **2007**, *100*, 303–315.
- Lynch, I.; Dawson, K. A.; Linse, S. Detecting Cryptic Epitopes created by Nanoparticles. *Sci. STKE* **2006**, *327*, pe14.
- Treuel, L.; Malissek, M.; Gebauer, J. S.; Zellner, R. The Influence of Surface Composition of Nanoparticles on Their Interactions with Serum Albumin. *ChemPhysChem* **2010**, *11*, 3093–3099.
- Casals, E.; Pfaller, T.; Duschl, A.; Oostingh, G. J.; Punter, V. Time Evolution of the Nanoparticle Protein Corona. *ACS Nano* **2010**, *4*, 3623–3632.
- Tsai, D.-H.; DelRio, F. W.; Keene, A. M.; Tyner, K. M.; MacCuspie, R. I.; Cho, T. J.; Zachariah, M. R.; Hackley, V. A. Adsorption and Conformation of Serum Albumin Protein on Gold Nanoparticles Investigated Using Dimensional Measurements and *in Situ* Spectroscopic Methods. *Langmuir* **2011**, *27*, 2464–2477.
- Monopoli, M. P.; Walczyk, D.; Campbell, A.; Elia, G.; Lynch, I.; Bombelli, F. B.; Dawson, K. A. Physical–Chemical Aspects of Protein Corona: Relevance to *in Vitro* and *in Vivo* Biological Impacts of Nanoparticles. *J. Am. Chem. Soc.* **2011**, *133*, 2525–2534.
- Nel, A.; Xia, T.; Mädler, L.; Li, N. Toxic Potential of Materials at the Nanolevel. *Science* **2006**, *311*, 622–627.
- Vecchio, G.; Galeone, A.; Brunetti, V.; Maiorano, G.; Sabella, S.; Cingolani, R.; Pompa, P. P. Concentration-Dependent, Size-Independent Toxicity of Citrate-Capped AuNPs in *Drosophila Melanogaster*. *PLoS One* **2012**, *7*, e29980.
- Vecchio, G.; Galeone, A.; Brunetti, V.; Maiorano, G.; Rizzello, L.; Sabella, S.; Cingolani, R.; Pompa, P. P. Mutagenic Effects of Gold Nanoparticles Induce Aberrant Phenotypes in *Drosophila Melanogaster*. *Nanomed. Nanotechnol. Biol. Med.* **2012**, *8*, 1–7.
- Chen, X.; Gambhir, S. S.; Cheon, J. Theranostic Nanomedicine. *Acc. Chem. Res.* **2011**, *44*, 841–841.
- Aubin-Tam, M.-E.; Hwang, W.; Hamad-Schifferli, K. Site-Directed Nanoparticle Labeling of Cytochrome C. *Proc. Natl. Acad. Sci. U.S.A.* **2009**, *106*, 4095–4100.
- Goobes, G.; Goobes, R.; Schueler-Furman, O.; Baker, D.; Stayton, P. S.; Drobny, G. P. Folding of the C-Terminal Bacterial Binding Domain in Statherin upon Adsorption onto Hydroxyapatite Crystals. *Proc. Natl. Acad. Sci. U.S.A.* **2006**, *103*, 16083–16088.
- Gray, J. J. The Interaction of Proteins with Solid Surfaces. *Curr. Opin. Struct. Biol.* **2004**, *14*, 110–115.
- Harding, M. M.; Nowicki, M. W.; Walkinshaw, M. D. Metals in Protein Structures: A Review of Their Principal Features. *Crystallogr. Rev.* **2010**, *16*, 247–302.
- Latour, R. A. Molecular Simulation of Protein–Surface Interactions: Benefits, Problems, Solutions, and Future Directions. *Biointerphases* **2008**, *it 3*, FC2–FC12.
- Cohavi, O.; Corni, S.; De Rienzo, F.; Di Felice, R.; Gottschalk, K. E.; Hoefling, M.; Kokh, D.; Molinari, E.; Schreiber, G.; Vaskevich, A.; Wade, R. C. Protein–Surface Interactions: Challenging Experiments and Computations. *J. Mol. Recognit.* **2009**, *23*, 259–262.
- Bachmann, M.; Goede, K.; Beck-Sickinger, A. G.; Grundmann, M.; Irbäck, A.; Janke, W. Microscopic Mechanism of Specific Peptide Adhesion to Semiconductor Substrates. *Angew. Chem., Int. Ed.* **2010**, *49*, 9530–9533.
- Di Felice, R.; Corni, S. Simulation of Peptide–Surface Recognition. *J. Phys. Chem. Lett.* **2011**, *2*, 1510–1519.
- Makrodimitris, K.; Masica, D. L.; Kim, E. T.; Gray, J. J. Structure Prediction of Protein–Solid Surface Interactions Reveals a Molecular Recognition Motif of Statherin for Hydroxyapatite. *J. Am. Chem. Soc.* **2007**, *129*, 13713–13722.
- Ghiringhelli, L. M.; Hess, B.; van der Vegt, N. F. A.; Delle Site, L. Competing Adsorption between Hydrated Peptides and Water onto Metal Surfaces: From Electronic to Conformational Properties. *J. Am. Chem. Soc.* **2008**, *130*, 13460–13464.
- Hong, G.; Heinz, H.; Naik, R. R.; Farmer, B. L.; Pachter, R. Toward Understanding Amino Acid Adsorption at Metallic Interfaces: A Density Functional Theory Study. *ACS Appl. Mater. Interfaces* **2009**, *1*, 388–392.
- Vila Verde, A.; Acres, J. M.; Maranas, J. K. Investigating the Specificity of Peptide Adsorption on Gold Using Molecular Dynamics Simulations. *Biomacromolecules* **2009**, *10*, 2118–2128.

34. Vila Verde, A.; Beltramo, P. J.; Maranas, J. K. Adsorption of Homopolypeptides on Gold Investigated Using Atomistic Molecular Dynamics. *Langmuir* **2011**, *27*, 5918–5926.
35. Coppage, R.; Slocik, J. M.; Briggs, B. D.; Frenkel, A. I.; Heinz, H.; Naik, R. R.; Knecht, M. R. Crystallographic Recognition Controls Peptide Binding for Bio-based Nanomaterials. *J. Am. Chem. Soc.* **2011**, *133*, 12346–12349.
36. Calzolari, A.; Cicero, G.; Cavazzoni, C.; Felice, R. D.; Catellani, A.; Corni, S. Hydroxyl-rich Sheet Adhesion to the Gold Surface in Water by First-Principle Simulations. *J. Am. Chem. Soc.* **2010**, *132*, 4790–4795.
37. Yu, J.; Becker, M. L.; Carri, G. The Influence of Amino Acid Sequence and Functionality on the Binding Process of Peptides onto Gold Surfaces. *Langmuir* **2012**, *28*, 1408–1417.
38. Feng, J.; Slocik, J. M.; Sarikaya, M.; Naik, R. R.; Farmer, B. L.; Heinz, H. Influence of the Shape of Nanostructured Metal Surfaces on Adsorption of Single Peptide Molecules in Aqueous Solution. *Small* **2012**, *8*, 1049–1059.
39. Hoefling, M.; Iori, F.; Corni, S.; Gottschalk, K. E. The Conformations of Amino Acids on a Gold(111) Surface. *ChemPhysChem* **2010**, *11*, 1763–1767.
40. Hoefling, M.; Iori, F.; Corni, S.; Gottschalk, K. E. Interaction of Amino Acids with the Au(111) Surface: Adsorption Free Energies from Molecular Dynamics Simulations. *Langmuir* **2010**, *26*, 8347–8351.
41. Hoefling, M.; Monti, S.; Corni, S.; Gottschalk, K. E. Interaction of β -Sheet Folds with a Gold Surface. *PLoS One* **2012**, *6*, e20925.
42. Toroz, D.; Corni, S. Peptide Synthesis of Gold Nanoparticles: The Early Steps of Gold Reduction Investigated by Density Functional Theory. *Nano Lett.* **2011**, *11*, 1313–1318.
43. Boisselier, E.; Astruc, D. Gold Nanoparticles in Nanomedicine: Preparations, Imaging, Diagnostics, Therapies and Toxicity. *Chem. Soc. Rev.* **2009**, *38*, 1759–1782.
44. Personick, M. L.; Langille, M. R.; Zhang, J.; Mirkin, C. Shape Control of Gold Nanoparticles by Silver Underpotential Deposition. *Nano Lett.* **2011**, *11*, 3394–3398.
45. Calzolari, A.; Franchini, F.; Gilliland, D.; Rossi, F. Protein–Nanoparticle Interaction: Identification of the Ubiquitin–Gold Nanoparticle Interaction Site. *Nano Lett.* **2010**, *10*, 3101–3105.
46. Kokh, D. B.; Corni, S.; Winn, P. J.; Hoefling, M.; Gottschalk, K. E.; Wade, R. C. ProMetCS: An Atomistic Force Field for Modeling Protein–Metal Surface Interactions in a Continuum Aqueous Solvent. *J. Chem. Theory Comput.* **2010**, *6*, 1753–1768.
47. Iori, F.; Di Felice, R.; Molinari, E.; Corni, S. GoLP: An Atomistic Force-Field to Describe the Interaction of Proteins with Au(111) Surfaces in Water. *J. Comput. Chem.* **2009**, *30*, 1465–1476.
48. Elechiguerra, J. L.; Reyes-Gasga, J.; Yacamán, M. J. The Role of Twinning in Shape Evolution of Anisotropic Noble Metal Nanostructures. *J. Mater. Chem.* **2006**, *16*, 3906–3919.
49. SDA, Simulation of Diffusional Association. <http://projects.villa-bosch.de/mcmsoft/sda/6.00/>. Accessed October 9, 2012.
50. Gabdouliline, R. R.; Wade, R. C. Effective Charges for Macromolecules in Solvent. *J. Phys. Chem.* **1996**, *100*, 3868–3878.
51. Kirkpatrick, S.; Gelatt, C. D.; Vecchi, M. P. Optimization by Simulated Annealing. *Science* **1983**, *220*, 671–680.
52. Brünger, A. T.; Adams, P. D.; Rice, L. M. New Applications of Simulated Annealing in X-ray Crystallography and Solution NMR. *Structure* **1997**, *5*, 325–336.
53. van der Spoel, D.; Lindahl, E.; Hess, B.; Groenhof, G.; Mark, A. E.; Berendsen, H. J. C. GROMACS: Fast, Flexible, and Free. *J. Comput. Chem.* **2005**, *26*, 1701–1718.
54. Lin, Y.; Pan, G.; Su, G.-J.; Fang, X.-H.; Wan, L.-J.; Bai, C.-L. Study of Citrate Adsorbed on the Au(111) Surface by Scanning Probe Microscopy. *Langmuir* **2003**, *19*, 10000–10003.
55. Kunze, J.; Burgess, I.; Nichols, R.; Buess-Herman, I.; Lipkowsky, J. Electrochemical Evaluation of Citrate Adsorption on Au(111) and the Stability of Citrate-Reduced Gold Colloids. *J. Electroanal. Chem.* **2007**, *599*, 147–159.
56. Brewer, S. H.; Glomm, W. R.; Johnson, M. C.; Knag, M. K.; Franzen, S. Probing BSA Binding to Citrate-Coated Gold Nanoparticles and Surfaces. *Langmuir* **2005**, *21*, 9303–9307.
57. Cohavi, O.; Reichmann, D.; Abramovich, R.; Tesler, A. B.; Bellapadrona, G.; Kokh, D. B.; Wade, R. C.; Vaskevich, A.; Rubinstein, I.; Schreiber, G. A Quantitative, Real-Time Assessment of Binding of Peptides and Proteins to Gold Surfaces. *Chem.—Eur. J.* **2011**, *17*, 1327–1336.
58. Fernandez, V. L.; Reimer, J. A.; Denn, M. M. Magnetic Resonance Studies of Polypeptides Adsorbed on Silica and Hydroxyapatite Surfaces. *J. Am. Chem. Soc.* **1992**, *114*, 9634–9642.
59. Mennucci, B.; Martnez, J. M. How to Model Solvation of Peptides? Insights from a Quantum Mechanical and Molecular Dynamics Study of *N*-Methylacetamide. 2. ^{15}N and ^{17}O Nuclear Shielding in Water and in Acetone. *J. Phys. Chem. B* **2005**, *109*, 9830–9838.
60. Zuiderweg, E. R. Mapping Protein–Protein Interactions in Solution by NMR Spectroscopy. *Biochemistry* **2002**, *41*, 1–7.
61. Peng, C.; Unger, S. W.; Filipp, F. V.; Sattler, M.; Szalma, S. Automated Evaluation of Chemical Shift Perturbation Spectra: New Approaches to Quantitative Analysis of Receptor–Ligand Interaction NMR Spectra. *J. Biomol. NMR* **2004**, *29*, 491–504.
62. Hong, G.; Heinz, H.; Naik, R. R.; Farmer, B. L.; Pachter, R. Toward Understanding Amino Acid Adsorption at Metallic Interfaces: A Density Functional Theory Study. *ACS Appl. Mater. Interfaces* **2009**, *1*, 388–392.
63. Tomasi, J.; Mennucci, B.; Cammi, R. Quantum Mechanical Continuum Solvation Models. *Chem. Rev.* **2005**, *105*, 2999–3093.
64. Cicero, G.; Calzolari, A.; Corni, S.; Catellani, A. Anomalous Wetting Layer at the Au (111) Surface. *J. Phys. Chem. Lett.* **2011**, *2*, 2582–2586.
65. Cappelli, C.; Mennucci, B. Modeling the Solvation of Peptides. The Case of (*s*)-*N*-Acetylproline Amide in Liquid Water. *J. Phys. Chem. B* **2008**, *112*, 3441–3450.
66. Structure-Based Chemical Shift Predictions. <http://casegroup.rutgers.edu/qshifts/qshifts.htm>. Accessed October 9, 2012.
67. Xu, X. P.; Case, D. A. Automated Prediction of ^{15}N , ^{13}Ca , ^{13}Cb and ^{13}C Chemical Shifts in Proteins Using a Density Functional Database. *J. Biomol. NMR* **2001**, *21*, 321–333.
68. Keller, R.; Grace, C. R.; Riek, R. Fast Multidimensional NMR Spectroscopy by Spin-State Selective Off-Resonance Decoupling (SITAR). *Magn. Reson. Chem.* **2006**, *44*, S196–S205.
69. Schmidt, J. M.; Howard, M. J.; Maestre-Martinez, M.; Perez, C. S.; Lohr, F. Variation in Protein C(alpha)-Related One-Bond J Couplings. *Magn. Reson. Chem.* **2009**, *47*, 16–30.
70. Gabdouliline, R. R.; Wade, R. C. Simulation of the Diffusional Association of Barnase and Barstar. *Biophys. J.* **1997**, *72*, 1917–1929.
71. Molecular and Cellular Modeling. www.h-its.org/mcm. Accessed October 9, 2012.
72. Baker, N. A.; Sept, D.; Joseph, S.; Holst, M. J.; McCammon, J. A. Electrostatics of Nanosystems: Application to Microtubules and the Ribosome. *Proc. Natl. Acad. Sci. U.S.A.* **2001**, *98*, 10037–10041.
73. H+++. <http://biophysics.cs.vt.edu/H++>. Accessed October 9, 2012.
74. Elcock, A. H.; Gabdouliline, R. R.; Wade, R. C.; McCammon, J. A. Computer Simulation of Protein–Protein Association Kinetics: Acetylcholinesterase–Fasciculin. *J. Mol. Biol.* **1999**, *291*, 149–162.
75. Jorgensen, W. L.; Maxwell, D. S.; TiradoRives, J. Development and Testing of the OPLS All-Atom Force Field on Conformational Energetics and Properties of Organic Liquids. *J. Am. Chem. Soc.* **1996**, *118*, 11225–11236.
76. Hess, B.; van der Vegt, N. F. Hydration Thermodynamic Properties of Amino Acid Analogues: A Systematic Comparison of Biomolecular Force Fields and Water Models. *J. Phys. Chem. B* **2006**, *110*, 17616–17626.

77. Frisch, M. J.; Trucks, G. W.; Schlegel, H. B.; Scuseria, G. E.; Robb, M. A.; Cheeseman, J. R.; Scalmani, G.; Barone, V.; Mennucci, B.; Petersson, G. A.; *et al.* *Gaussian 09*, revision C.01; Gaussian, Inc.: Wallingford, CT, 2010.
78. Mennucci, B.; Cancés, E.; Tomasi, J. Evaluation of Solvent Effects in Isotropic and Anisotropic Dielectrics and in Ionic Solutions with a Unified Integral Equation Method: Theoretical Bases, Computational Implementation, and Numerical Applications. *J. Phys. Chem. B* **1997**, *101*, 10506–10517.
79. Cancés, E.; Mennucci, B.; Tomasi, J. A New Integral Equation Formalism for the Polarizable Continuum Model: Theoretical Background and Applications to Isotropic and Anisotropic Dielectrics. *J. Chem. Phys.* **1997**, *107*, 3032–3041.
80. Tomasi, J.; Mennucci, B.; Cammi, R. Quantum Mechanical Continuum Solvation Models. *Chem. Rev.* **2005**, *105*, 2999–3093.